Volume 9
World Scientific Series in Nanoscience and Nanotechnology

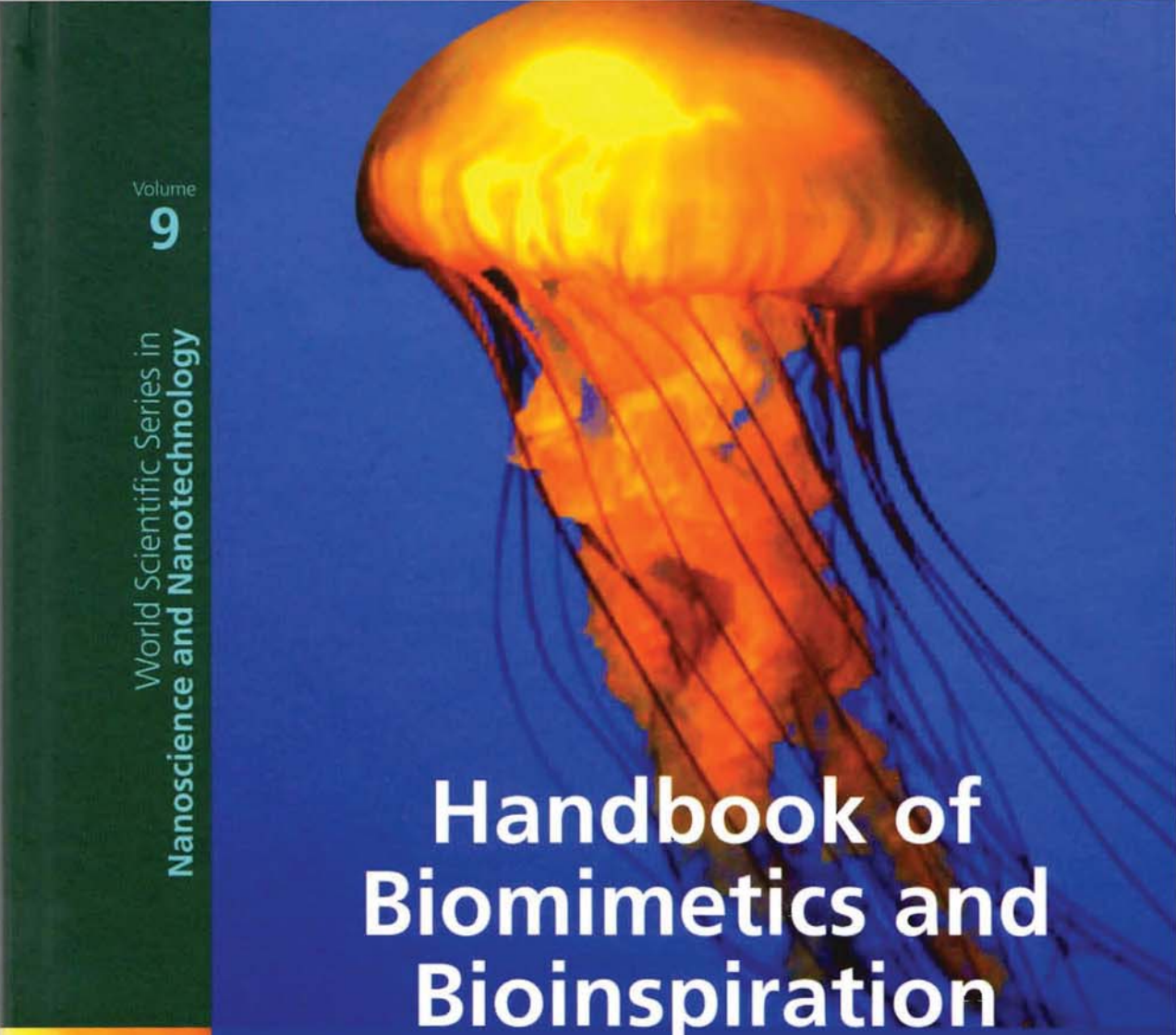

Handbook of Biomimetics and Bioinspiration

❷ Electromechanical Systems

Edited by
Esmaiel Jabbari *editor-in-chief*
Deok-Ho Kim • Luke P Lee
Amir Ghaemmaghami • Ali Khademhosseini

World Scientific

Chapter 31

HAIR-BASED FLOW-SENSING INSPIRED BY THE CRICKET CERCAL SYSTEM

G. J. M. Krijnen, H. Droogendijk, T. Steinmann, A. Dagamseh,
R. K. Jaganatharaja and J. Casas*

MESA+ Institute for Nanotechnology,
University of Twente, Enschede, The Netherlands
**Institut de Recherche en Biologie de l'Insecte,*
Université de Tours, Tours, France

micro electro mechanical system (MEMS) offers exciting possibilities for the fabrication of bioinspired mechanosensors. Over the last years we have been working on cricket inspired hair-sensor arrays for spatio-temporal flow-field observations (i.e., flow-cameras) and source localization. Whereas making flow-sensors as energy efficient as cricket hair-sensors appears to be a real challenge, we have managed to fabricate hair-sensors with sub-millimeter per second flow sensing thresholds, use them in lateral line experiments, address them individually while in arrays, track transient flows, quantify viscous coupling effects and use parametric effects to achieve sharp filtering and amplification. In this research insect biologists and engineers have been working in close collaboration, generating a bidirectional flow of information and knowledge, beneficial to both. For example where the engineering has greatly benefitted from the insights derived from biology and biophysical models, the biologists have taken advantage of MEMS structures allowing for experiments that are hard to do on living material.

1. Introduction

The filiform hairs of many insects, spiders and other invertebrates are among the most delicate and sensitive flow sensing cells: they measure displacement of less than a hydrogen diameter (sensitivity ca. 10^{-10} m = 1Å) and react to flow speed down to 30 μm/s. If one considers the energy needed to trigger a cell reaction, one finds that they react with a thousandths of the energy contained in a photon, so that they surpass photoreceptors in energy sensitivity. In fact, these mechanoreceptors work at the thermal noise level.[1] These hairs pick up air velocity, implying that they measure both the direction and speed of air flow, in contrast to pressure receivers,

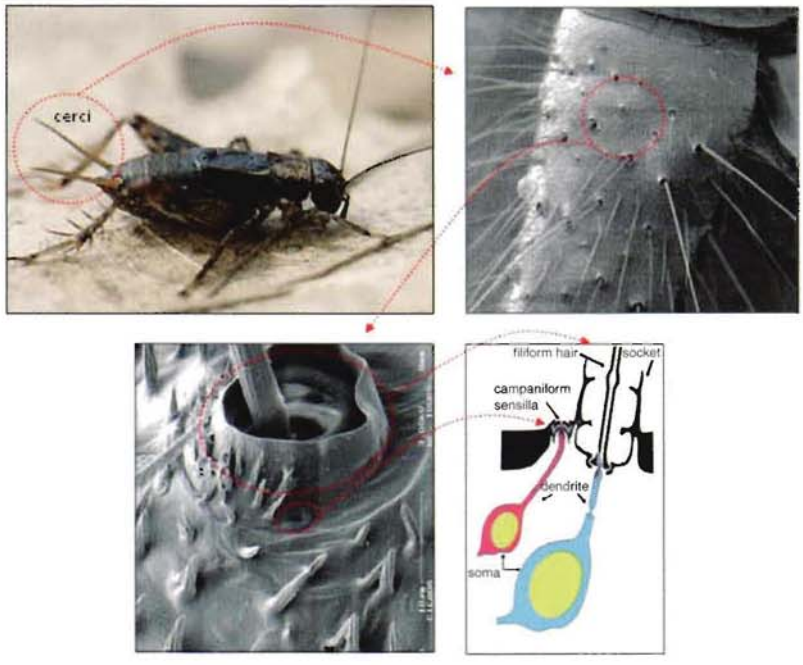

Fig. 1. Illustration of the hair-sensory system of crickets.

i.e., ears. Since several decades the biomechanics of the filiform hairs have been studied with care by several groups worldwide, based on the analogy with a single degree of freedom inverted pendulum (see, e.g., the review of hair biomechanics in Ref. [2]).

Among insects, mainly cockroaches and crickets have been studied, because their air flow sensitive hairs are put on two antenna-like appendages, the cerci (cercus in singular). Insect hairs usually have a high aspect ratio, with a length of a few hundreds of microns up to 2 mm, and with a diameter of less than a dozen microns (Fig. 1). Their longitudinal shape is conical which has been found to have an influence on the drag forces. Hairs and sockets are ellipsoidal in cross-section, which leads to a preferential direction of movement. The base of the hairs is complex, and its mechanics poorly understood. In crickets, only a single sensory cell is below the hair shaft (Fig. 1).

Single hairs, or groups of hairs, are not placed at random on the body.[3,4] To the same extent that the exact shape of hairs as well as their relative position within a group have been molded by natural selection, the position of the hairs on the sensory organ has been exposed to natural selection too. This aspect of mechanosensory research is however badly neglected. As for the positions along the cercus, the presence of a potential acoustic fovea (i.e., a location with particularly high acuity)

at the base of the cercus has been hinted at, not only due to the highest hair density in this region, but also because it corresponds to the region with the largest flow velocities, the cercus being the largest there. Putting hairs radially around the cercus enables crickets also to pick up transversal flows, for which the peak flow velocities are larger than in the situation where the hairs would be placed on a flat surface; in the latter case, hairs are submitted to longitudinal flow with lower peak velocities.[5] In summary, where you put your sensors relative to your body geometry matters a lot.

An action potential triggered by a moving hair ends up in the terminal abdominal ganglion (TAG), a local neuronal processing unit. Information from all the hairs, as well as from other sensors, converges there and is processed by interneurons. The convergence of information at this stage is enormous: the afferent neurons of about 1500 hair-sensors are connected to only some 20 interneurons.[6] The fact that invertebrates possess few large, singly identifiable neurons enabling comprehensive mapping and repeated recordings of activities is a unique asset which explains the interest in such exotic systems. Information coming from the central brain as well as from the higher ganglia also descends into the TAG. Once processed, the combined information moves up quickly towards higher neuronal centers, in particular the ganglia in which the hindleg movements are being decided. This local feedback loop, with little input from the main brain, enables the animal to process vital information and act accordingly very quickly. As so often with invertebrates, what can be processed locally should be done so, a distributed processing scheme exemplifying why biomimetism has so much to gain from this group of animals.

The last level of integration is behavior, and flow sensing is known to be of importance in predator and prey perception, sexual selection and most likely other context, such as noticing its own speed and movement. Predator avoidance is obviously a major selection force, where speed is of paramount importance. Jumping or running away is the behavior which is elicited using appropriate stimuli. The cricket possesses in the TAG an internal map of the direction of the stimuli from the outside world and the determination of the geometric direction of incoming flow by the cercus has been described in one of the nicest case studies of spatial representation.[6] Computing the speed of an approaching predator is also carried out by the TAG, and has been only recently established using appropriate stimuli.[7] Where to jump is a different question, in which directing stimuli and other conditions intervene.

Natural selection acts along the full chain of information transfer, from acquisition and processing, up to actuation. This is important to restate in a biomimetic context, as the extreme sensitivity on the biomechanical side of the hair shaft, which has been almost the exclusive focus of the engineer's attention, could be otherwise

lost into an inefficient sequence of information transfer. As of today, we have however very little information about the constraints acting on the different parts of the chain, and hence no idea about their optimization.

2. Hair-Sensors

2.1. *Flow as information source*

Whereas for humans (mammals) flow may not seem a very information rich modality for probing the environment, nature seems to have numerous examples of species that exactly do this. To put this in perspective it may be helpful to look at the fields produced by a harmonically moving sphere (dipole), which, with some simplifications, may resemble more natural sources such as wing-beats of flying insects or tail movements of fish. Obviously the fields produced by a dipole entail both pressure and flow fields. Depending on the medium, e.g., water or air, in which the dipole resides, and more specifically on the compressibility of the medium, it may seem that pressure and flow could play comparably important roles, albeit that flow-fields inherently carry directional information (being vector-fields) whereas pressure is a scalar field only. Although this observation may be true at relatively long distance[a] where the ratio of flow- and pressure fields becomes constant, near to the source flow-fields are 'comparatively stronger'. This is shown in Fig. 2 left, where on-axis pressure and velocity, normalized to their respective values at $k \cdot r = 1$ (with k the wavenumber and r the distance), are plotted as a function of normalized distance. The situations of compressible (solid lines) as well as incompressible (dashed lines) media, as calculated using the expressions of Lamb,[8] are shown.

The ratio between pressure and flow velocity (which would be the acoustic impedance for compressible media) equals $j\rho\omega r/2$ (ρ being the density, ω the angular frequency) for $k \cdot r < 1$ indicating that pressure becomes comparatively small for shorter distances and lower frequencies. As an illustration: the interaction of a flying wasp with a wing beat of about 150 Hz with, say, a caterpillar,[10] the condition $k \cdot r = 1$ corresponds with $r \approx 0.34$ m, which is a relative large distance as compared to body lengths of the animals.

2.2. *Hair-sensor physics*

There have been a few seminal papers (e.g., Refs. [11] and [12]) describing the interaction of harmonic flows with hairs. In general the relative flow velocities (v_r)

[a]For compressible media one could think of at least a few wavelengths away from the source).

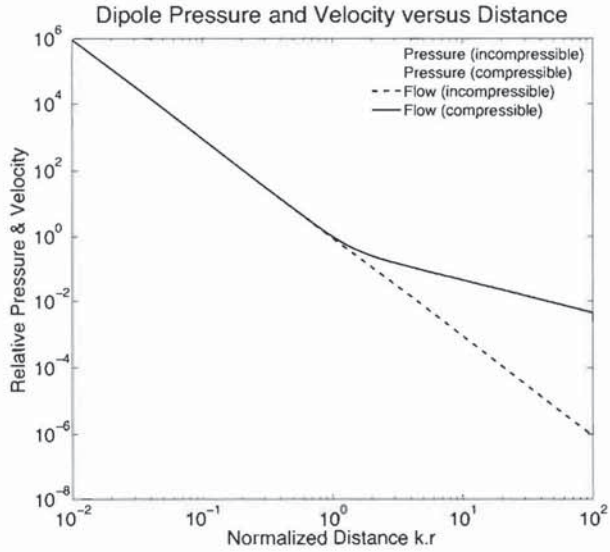

Fig. 2. Theoretical dipole-field flow (blue) and pressure (green) as function of normalized distance. Clearly, for $k \cdot r \leq 1$, i.e., distances smaller than the wavelength divided by 2π, there are only minor differences between the results of compressible and in-compressible theory, a fact that can be readily exploited when modeling relative complex aerodynamic predator–prey interactions.[9]

have been assumed to be small which, in combination with the small hair diameters (d), yields rather small Reynolds ($\mathrm{Re} = v_r d/\nu$) numbers. Moreover, the frequencies are limited to a few 100 Hz causing the Strouhal number ($St = \omega d/2v_r$) to be small as well. For a hair-diameter of 25 μm to 50 μm, an air-oscillation frequency of 250 Hz and a flow-velocity amplitude of 10 mm/s, Re varies between 0.008 and 0.016 and St between 1.96 and 3.92 (for the flow around the hairs).

Assuming that the flow $v(t)$ is oscillating over a flat surface, the so-called no-slip boundary-condition[b] gives rise to the height y-dependent velocity profile[13]:

$$v(t) = V_0 \sin(\omega t) - V_0 e^{-\beta y} \sin(\omega t - \beta y), \tag{1}$$

where β is proportional to the reciprocal of the boundary layer thickness, with ν the kinematic viscosity ($\beta = \sqrt{\omega/2\nu}$). Using trigonometric identities, the velocity profile can be expressed as a sinusoidal function with an amplitude V_y and phase shift ζ_y:

$$v_y(t) = V_y \sin(\omega t + \zeta_y), \tag{2}$$

[b]The *no-slip boundary-condition* refers to the situation where it may be expected that, due to viscosity, the medium is at rest at the interface with the substrate.

where

$$V_y = V_0\sqrt{1 + e^{-2\beta y} - 2e^{-\beta y}\cos(\beta y)} \quad \text{and}$$
$$\zeta_y = \arctan\left(\frac{e^{-\beta y}\sin(\beta y)}{1 - e^{-\beta y}\cos(\beta y)}\right). \tag{3}$$

The rather small Reynolds numbers and the large hair-length to hair-diameter ratio allow the use of the Stokes expressions for the drag-torque exerted by the harmomic air-flow on the hairs.[14] Further, since our artificial hair-sensors are mounted on flat substrates and follow the previously described flow profile, the relative flow velocity v_r can be related to the drag force per unit length F_d as[11]:

$$F_d(t) = 4\pi\mu G \cdot v_r(t, y) + \left(\frac{\pi\rho d^2}{4} - \frac{\pi^2\mu G}{g\omega}\right)\frac{dv_r(t, y)}{dt} \tag{4}$$

with ρ the medium density and μ the medium dynamic viscosity. In these equations, G and g are dimensionless parameters:

$$G = \frac{-g}{g^2 + (\pi/4)^2}, \quad g = \gamma + \ln(s), \quad s = \frac{d\beta}{2\sqrt{2}}, \tag{5}$$

where the dimensionless parameter $s \ll 1$, and d is the hair diameter.

Mechanically, the hair-sensor can be understood as a so-called inverted pendulum; a second-order rotational-mechanical system with moment of inertia I due to the hair, a rotational stiffness S, a rotational damping R and a flow induced drag-torque $T(t)$ (Fig. 3). The air-flow generates a torque on the hair-shaft, primarily

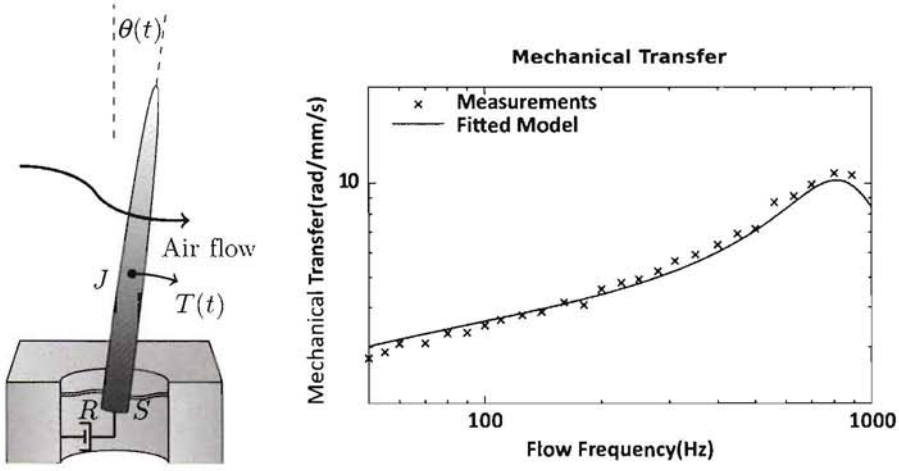

Fig. 3. Left: Model of a flow sensing hair based on an inverted pendulum (adapted from Ref. [12]). Right: Prediction (solid line) of the model and measured mechanical response (crosses).

by viscous drag since at the velocities and geometries normally encountered pressure drag is small. Note that under most conditions artificial hairs can be assumed infinitely stiff and that the rotation angles are rather small (of the order of 1 to 10 mrad amplitude per m/s flow-velocity amplitude). By taking into account that the drag-torque depends on the relative velocity v_r, i.e., the difference in flow- and hair-velocities, the total system's governing differential equation is given by[2]:

$$(J + J_\rho + J_\mu)\frac{d^2\theta(t)}{dt^2} + (R + R_\mu)\frac{d\theta(t)}{dt} + S_0\theta(t) \tag{6}$$

$$= 4\pi\mu G \int_0^L v_y(t)y\,dy + \left(\frac{\pi\rho d^2}{4} - \frac{\pi^2\mu G}{g\omega}\right)\int_0^L \frac{dv_y(t)}{dt}y\,dy. \tag{7}$$

The quantities J_ρ and J_μ are often referred to as virtual added mass and R_μ as the virtual added damping[2]:

$$J_\rho = \frac{\pi\rho d^2 L^3}{12}, \quad J_\mu = -\frac{\pi^2\mu G L^3}{3g\omega} \quad \text{and} \quad R_\mu = \frac{4}{3}\pi\mu G L^3. \tag{8}$$

Using the approach given by Ref. [12] the angular deflection amplitude Θ_m for an oscillating air-flow with frequency ω is given by:

$$\Theta_m = \frac{\sqrt{A^2 + B^2}}{\sqrt{[S_0 - (J + J_\rho + J_\mu)\omega^2]^2 + [(R + R_\mu)\omega]^2}} \tag{9}$$

and the phase shift ϕ_m with respect to the oscillating air-flow as:

$$\phi_m = \arctan\left(\frac{B[S_0 - (J + J_\rho + J_\mu)\omega^2] - A(R + R_\mu)\omega}{A[S_0 - (J + J_\rho + J_\mu)\omega^2] + B(R + R_\mu)\omega}\right), \tag{10}$$

where

$$\begin{aligned} A &= \int_0^L |Z_S| V_y y \cos(\zeta_y + \arg(Z_S))\,dy \\ B &= \int_0^L |Z_S| V_y y \sin(\zeta_y + \arg(Z_S))\,dy \end{aligned} \tag{11}$$

with

$$Z_S = 4\pi\mu G + j\frac{\pi\rho d^2}{4}\omega - j\pi^2\mu G. \tag{12}$$

Numerical evaluation of the drag-torque exerted on a hair (cf. Eqs. (9) and (11)), for hair geometries that resemble those of our artificial hair-sensors, shows that the torque amplitude is approximately proportional to the length of the hair cubed, when the hair is shorter than the boundary layer thickness, and proportional with hair-length squared once the hair is longer than the boundary layer thickness (see Fig. 5 left). On the other hand, the dependence of the angular amplitude on the diameter of the hairs is rather small (see Fig. 5, right). These results have important impact on optimization of the artificial hair-sensors.

2.3. *Hair-sensor design*

From a biological viewpoint one may want to understand the entanglement of the geometric and physical parameters of the hair-sensor system *as they are*. However, from an engineering viewpoint things look slightly different since (a) not all the details and interplay of all the involved parameters of the insects hair-sensor system are known (i.e., plain mimicking of the cricket cercal system is no option) and (b) micro electro mechanical system (MEMS) fabrication technology offers a latitude of size possibilities and material choices that only partly overlaps the natural system (cf. Figs. 1 and 4). Therefore, the value of various design parameters needs to be determined from other analyses.

2.3.1. *Hair length and boundary layer*

The length of the hairs (L) plays a dominant role in the overall performance of the hair-sensors. Obviously, when exposed to a uniform flow the total drag-torque on cylindrical hairs would increase proportional with the hair-length squared. However, due to the frequency depending boundary layer the drag-torque first increases with

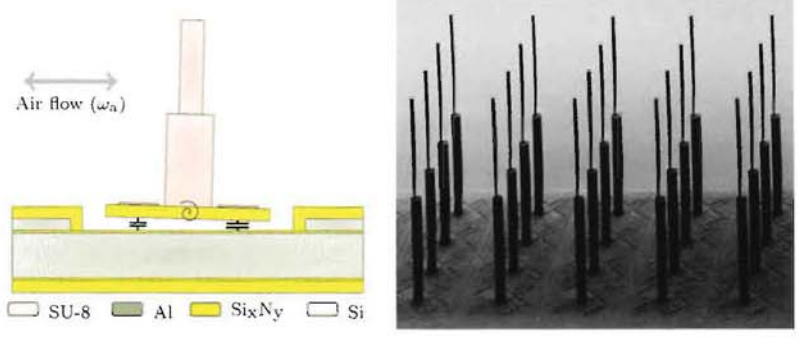

Fig. 4. Left: Schematic of the artificial hair-sensors using differential capacitive read-out. Right: Scanning Electron Micrograph (SEM) of a realized hair-sensor array.

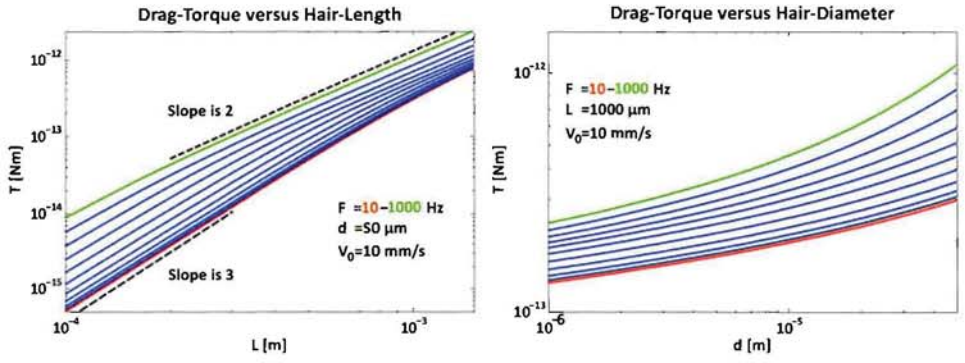

Fig. 5. Drag-torque as predicted by Stokes equations for hair-geometries comparable to our artificial hairs. Left: Drag-torque versus hair-length. Right: Drag-torque versus hair-diameter.

the third power of hair-length up to about δ_b and then follows a quadratic dependence (see Fig. 5, left). But at the same time the hair inertial moment (J) is of order $O(L^3)$.

2.3.2. *Hair diameter and viscous drag*

When increasing the diameter of the hairs (d) the resulting drag-force will increase as well (see Fig. 5, right). Numerical evaluation of the Stokes expressions for drag-force shows that the dependence on diameter is weak in the range of interesting hair-diameters; on the order of $O(d^{1/3})$. At the same time the hair moment of inertia is of order $O(d^2)$, negatively affecting the resonance frequency (i.e., bandwidth). Therefore it is beneficial to have thin hairs. Technologically it turns out to be rather difficult to make hairs with aspect ratios of more than about 10–20. We have tackled this problem by segmenting our artificial hairs with a lower part diameter of 50 μm and a top part diameter of 25 μm, reducing the hair inertial moment by about 65%.[15]

2.3.3. *Torsional stiffness*

Obviously, when looking for the largest rotation angle for any given drag-torque one may want to choose the lowest possible torsional stiffness (S). But for given hair inertial moment a reduction of S also leads to a reduction of the resonance frequency which is given by $\omega_0 = \sqrt{S/J}$.

2.3.4. *Damping*

Damping of the hair-sensors comes in various forms. For the crickets the hair-sockets provide some torsional damping (R) by visco-elastic material properties (see Ref. [16] for such material properties in spider hair mechano sensors) whereas

for the artificial hair-sensors torsional damping is caused by both material as well as squeeze film damping due to the small gap between the silicon-nitride plates and the substrate. On top of these damping contributions the hairs themselves incur damping by viscous forces when the hairs move relatively to the surrounding air. In the case of crickets, the total damping seems to be appropriately controlled[17] by the organism yielding hairs that are approximately critically damped. It is hypothesized that mechanical impedance matching helps the sensors to obtain maximum energy from the surroundings.[12] On the other hand, a critically damped second-order system also exhibits minimum response time with respect to (transient) flows. Nevertheless, the evolutionary pressures driving the appropriate damping for cricket hair-sensors have not yet been identified. In the artificial hair-sensors, except for adding specific holes to the membranes to tailor the squeeze film effects, not much can be done to optimize the damping without far-reaching consequences for the fabrication technology.

2.3.5. *Torsional spring material*

The mechanical sensitivity of our hair-sensors is currently about 2 orders of magnitude less than those of crickets, primarily due to a much larger rotational stiffness: $1.5 \cdot 10^{-11}$ Nm/rad for crickets versus $\approx 5 \cdot 10^{9}$ Nm/rad for our sensors. But reducing the torsional stiffness comes with two difficulties. In order to conserve bandwidth the moment of inertia of the hairs needs to be further reduced. The second complication is that the suspension beams provide torsional (S) as well as vertical stiffness (K). Both decrease with increasing length l but S decreases with $O(l^{-1})$ whereas K decreases with $O(l^{-3})$. The result is that a large rotational compliance combined with a large vertical stiffness can only be obtained using compliant materials, i.e., with low Young's modulus and appropriate beam-cross-sections. A nice reference to the flexible materials often encountered in nature (despite the fact that our torsional suspension and the cricket hair-sockets have little in common).

2.3.6. *Figure of Merit*

Optimization of our hair-sensors has been driven by a Figure of Merit (FoM), basically being the product of mechanical responsivity and bandwidth[18]: $\text{FoM} = \sqrt{L/\rho S d^{4/3}}$. This has emphasized what could be learned directly from observation of cricket hair-sensors, i.e., that hairs should be long and thin, and mounted on very compliant suspensions. However, with respect to damping the optimum damping factors still need to be identified. Compared to crickets, for a 1 mm long hair the FoM of our hair-sensors is about a factor of 70 smaller due to the larger rotational stiffness and thicker hairs.

2.3.7. *Capacitive read-out*

The angular rotations induced by harmonic flows normally encountered are rather small: on the order of 1 mrad/mm/s. Therefore, the capacitive read-out needs to be judiciously implemented. Our hair-sensors are based on a differential read-out, using a 1 MHz interrogation signal, a charge amplifier and a multiplier to retrieve the base-band information. Since parasitics due to bond-pads and wires are relatively large the fractional capacitance changes, which ultimately determine the sensitivity of the sensor, need to be optimized. Because the sensor's membrane area close to the rotational axis does not generate much capacitance change the membrane should primarily be long. Also, the smaller the effective gap (g) between the capacitor electrodes, the larger the effect. Eventually the fractional capacitance change is given by $\partial C/\partial\alpha \times 1/C = l/g$, giving clear directions for optimization. Early generations of our sensors were affected with stress-induced upward curvature of the membranes, negatively influencing the capacitive sensitivity. In later generations aluminum is used as electrode material since it has a high electrical conductivity (and therefore the layer can be thin), has a low Young's modulus (thus will cause relative little bending) and can be deposited at low temperatures (reducing residual thermal stress).

The latest generation of our artificial hair-sensors is based on silicon-on-insulator (SOI) technology (see Fig. 13 left) which helps to reduce parasitic capacitances. The performance of this type of sensors is shown in Fig. 6 where results are displayed for a single hair-sensor. The threshold flow-amplitude value is at about 1.00 mm/s to 1.25 mm/s for frequencies between 100 Hz to 400 Hz and is currently limited by electronics noise (thermal-mechanical noise is predicted to be more than two order

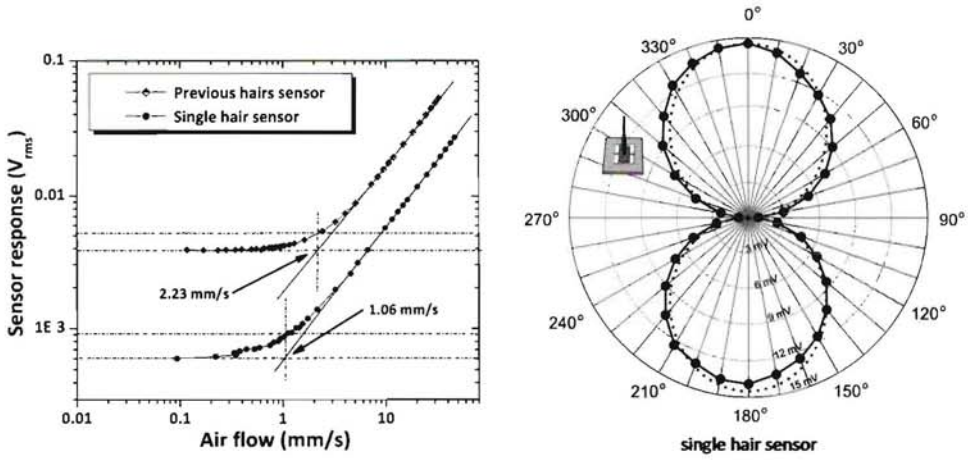

Fig. 6. Single hair-sensor flow-amplitude threshold at 250 Hz (left, lower curve) and directivity[19] (right).

of magnitude smaller). The sensors also exhibit a strong and clear directivity pattern, which closely matches a theoretically ideal figure of eight.[19]

2.4. *Optimization of hair geometry*

The artificial hairs on top of the sensor membranes are the mechanical interfaces that cause the flow information to result in membrane rotations inducing capacitance changes which are eventually transformed into equivalent electrical signals. Making long hairs in micro-fabrication technology is by no means an easy challenge since both the absolute length as well as the aspect ratio of these structures are non-standard for MEMS. Hence, over the years various technologies have been investigated to fabricate optimal hairs.

2.4.1. *Importance of hair shape*

For the effective operation of our artificial hair sensors, the shape of the SU-8 hair plays a central role. The hair geometry serves two basic purposes: (i) it determines the amount of flow-induced drag-torque acting upon the hair and (ii) it contributes to the mass moment of inertia, which determines the mechanics of the sensory system. Finding the optimum balance between the drag-torque reception and the hair moment of inertia has been the primary motivation for such optimization.

Taking a closer look at the shape of cercal filiform hairs themselves, could guide towards the first steps of hair shape optimization. The hairs on the cerci are found to appear in a wide range of lengths from 30 μm to 1500 μm with diameters occurring from 1 μm to 9 μm.[11] Initially, the structural effects of the cercal hairs were analyzed by assuming a cylindrical[11] or linearly tapered conical shape.[20] But upon accurate measurements the hair shape was found to be parabolically elongated, i.e., the hair-diameter increases with the square-root of the distance from their tip.[12] Earlier electron microscope studies showed the hairs to be hollow tubes, with the diameter of the inner hollow cavity being approximately one-third of the outer diameter.[21] The elongated-paraboloid shape of the filiform hairs apparently strikes a fine balance between the drag-torque reception capability and its moment of inertia. The goal is, thus, to fabricate artificial hairs which closely resemble the natural filiform hairs.

2.4.2. *Artificial hairs: Past and present*

Artificial hairs were initially fabricated by etching structures on bare silicon wafers and conformally covering them with silicon nitride using low-pressure chemical vapor deposition (LP-CVD). Upon selectively etching the silicon substrate, silicon nitride hairs were uncovered (Fig. 7).[22] These hairs were very complex to be integrated into a functional sensor. Subsequent generations of our sensor arrays

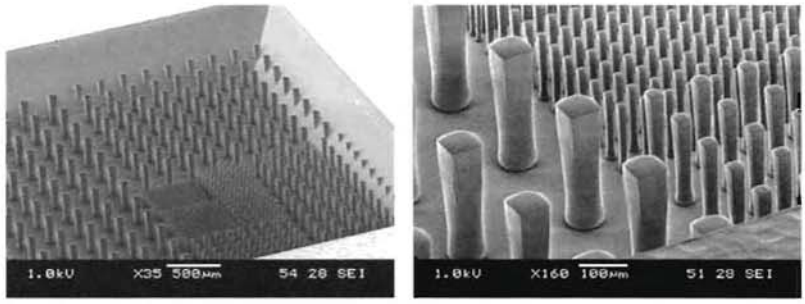

Fig. 7. Initial attempts to make hairs were based on Deep Reactive Ion etching in silicon with subsequent conformal nitride overgrowth and silicon removal. Left: overview. Right: further magnification of the same hairs illustrating the effects of anisotropy in dry etching.

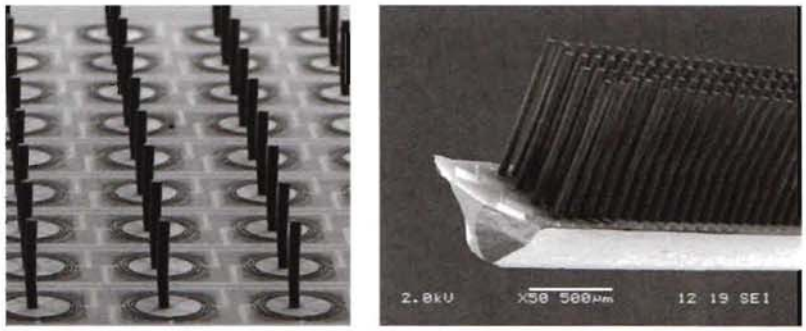

Fig. 8. First (left) and second (right) generation artificial hair-sensors.

comprised artificial hairs made of SU-8, a negative-tone, epoxy-based photoresist, fabricated by means of standard lithography. First, a single layer of SU-8 photoresist was used resulting in hairs of about 450 μm length[23] (Fig. 8, left). In later generations of our hair sensors, two subsequent layers of SU-8 were spun and hairs of length of up to 900 μm were photo-patterned by top-side exposure (Fig. 8, right). The result was that hairs were long and had a cylindrical shape with a uniform diameter of about 50 μm.

For the current generation of artificial hairs (Fig. 4), a new geometry was chosen in order to reduce the hair moment of inertia. The idea is to fabricate artificial hairs in two parts (i.e., two layers of SU-8 photoresist), where the hair diameter of the top is half as large as the diameter of the bottom part. Such hair geometry effectively reduces the hair moment of inertia up to 65%.

One of the difficulties in using multi-spun SU-8 layers for artificial hairs is that alignment of structures on the subsequent layers becomes critical. However, this issue can be overcome by using bottom side lithography for achieving proper alignment between both layers. Further, the standard top-side exposure of SU-8

lithography limits us to achieve hair length variations within an array to only up to 2 or 3. Therefore, in addition to fabricate artificial hairs with nature-like shape, a new and less-complex fabrication technology is sought in order to realize hairs of varying hair lengths in a wider range, all within the same array.

2.4.3. *Nature-like hairs: Future?*

Bottom-side exposure of SU-8 layers is a well-known technique, e.g., commonly used as molds in the fabrication of micro-needle arrays for drug-delivery applications.[24–26] For our requirements, we used the above-mentioned bottom-side exposure for fabricating hairs with gradually tapering tips aimed to resemble the shape of actual filiform hairs of cerci. A simple, proof-of-concept process flow was developed. For the fabrication, a patterned Aluminium layer with circular openings on top of a standard glass substrate is used. Two layers of SU-8 are spun to a thickness of 900 μm to 1000 μm, after which the glass substrate is flipped and exposed through the circular openings. Upon development of the SU-8 layer, nature-like SU-8 hairs, resembling their natural counter-parts closer compared to previous versions of our artificial hairs (Fig. 9, left) were created. Further, the variations in circular opening diameters of the patterned aluminium layer allowed us to achieve a wide range of hair length variations, all in a single step of photolithography (Fig. 9, right).

The fabricated nature-like hair samples were analyzed to find the optimal exposure time and the effect of different design parameters of the aluminium pattern on the hair geometry. Moreover, from the resulting hair-shapes and the Stokes drag-force expressions the drag-torque was estimated and from the shapes and the density of SU-8 the moment of inertia of the hairs was calculated. The ratio of both quantities is shown in Fig. 10. The models predict that the nature-like hairs form an

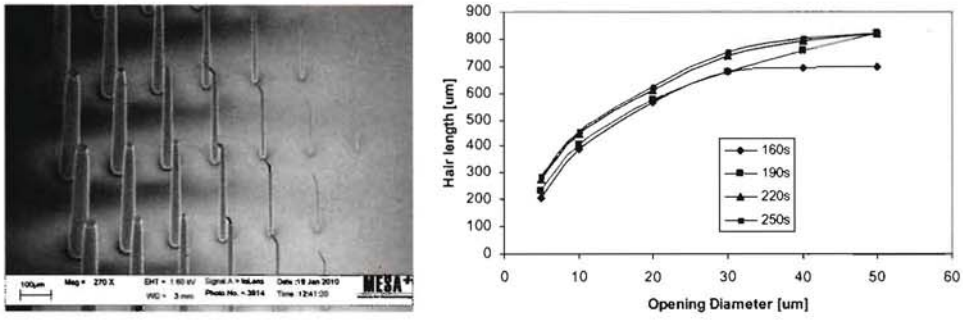

Fig. 9. SEM image of nature-like hairs (left) with variations in hair-length determined by the diameter of the open circles used for exposure (right). The process is slightly dependent on illumination time but still sufficiently robust.

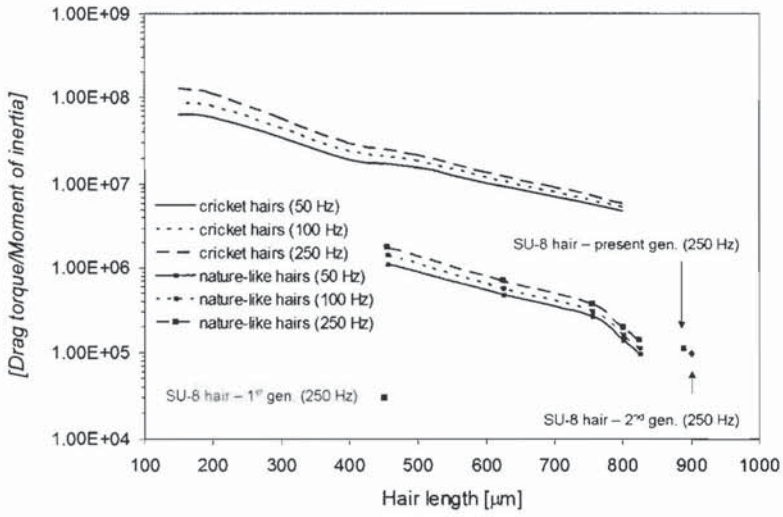

Fig. 10. Ratio of induced drag-torque over moment of inertia for various artificial hair-generations and cricket hairs. The latter were calculated using the allometric scaling and material properties as introduced by Shimozawa.[12]

improvement of up to a factor of 10 relative to the current hair-generation, but still lacking up to 2 orders relative to cricket hairs.

The remaining challenge is to develop a new process scheme to integrate the nature-like SU-8 hairs into the existing sensor fabrication flow. The process flow for wafer-through etch-holes on the silicon wafers for back-side exposure and the applicability of aluminium as both capacitor electrode and hair mask should be tested and optimized.

3. Viscous Coupling

Arthropods are often quite hairy, and the high density of flow sensing hairs implies that these hairs interact with each other. The hydrodynamical interactions between hairs, called viscous coupling, have been studied only recently and were found to be highly dependent on the geometrical arrangement of hairs, of their respective lengths and preferential planes of movement, as well as on the frequency content of the input signal.[27] Hairs often interact over long distances, up to 50 times their radius, and usually negatively. Short hairs in particular 'suffer' substantially from the presence of longer hairs nearby. However, positive interactions, where the flow velocity at one hair is increased by the presence of nearby hairs, have been observed in real animals and reproduced computationally.[28] The biological implications of these interactions have only recently been addressed, and hint towards a coding of incoming signals which relies strongly on the specific sequence of hairs being triggered.[29]

In other words, the signature of the incoming signal may be mapped into a given sequence of recruited hairs, which in turn produces a typical sequence of action potentials.

On the physical level it is rather hard to determine viscous coupling effects on real animals due to the pseudo randomness of hair-position, hair-length and hair-orientation. Here the MEMS capabilities to fabricate regular structures with well-defined inter-hair distances present a way to tackle the problem, see Fig. 11. We have made various structures to systematically investigate viscous coupling effects. Both the flow-profiles[27] as well as the hair-rotations in the presence of perturbing hairs[30] have been studied. An illustration of the effects of shorter inter-hair distances on flow profiles can be seen in Fig. 12, left. The flow-velocities were determined for harmonic flows over a tandem of two MEMS-fabricated hairs by particle image velocimetry (PIV). Figure 12, right — top, shows a frequency response of a hair-sensor with 2 perturbing hairs (black), 1 perturbing hair (red) and no perturbing hair (blue). The hair sensors spacing was about 2.1 times the hair diameter. Clearly, with one or two perturbing hairs the hair-rotations are smaller than without perturbing hairs. Right — bottom: frequency dependence of the viscous coupling constant for 2 versus 0 perturbing hairs (black), 2 versus 1 perturbing hair (red) and 1 versus 0 perturbing hairs (blue). Lines are predictions based on a modified version of the model introduced in Ref. [31], for the case of arrested hairs, dots are measurements with uncertainty intervals.

4. Array-Sensing

The SOI based technology (Fig. 13, left) not only serves to reduce parasitics but also allows for crossing electrodes since both the silicon device-layer of the SOI wafer as well as the top aluminium layer, mutually separated by silicon-nitride, allow for electrical connections. The technology enables frequency division multiplexed (FDM) interfacing to individual sensors in a rectangular array, reducing the number of required electrode connections from $3(n \times m)$ to $2n + m$ for a $n \times m$ array of hair-sensors.[34] Further, this scheme retains the SNR of the hair-sensors at the level they would have had when each single hair-sensor had been individually connected. See Fig. 13, right.

The FDM technique allows for real-time read-out of many sensors in parallel. Therefore, it enables the observation of spatio-temporal flow-patterns in which the details carry information of the source of the field, i.e., this type of flow-sensor array in principle allows for the observation (of the movement) of objects in the near-field environment, thus acting as a flow-camera. Figure 14, left, shows an array of sensors, each individually interfaced by FDM.

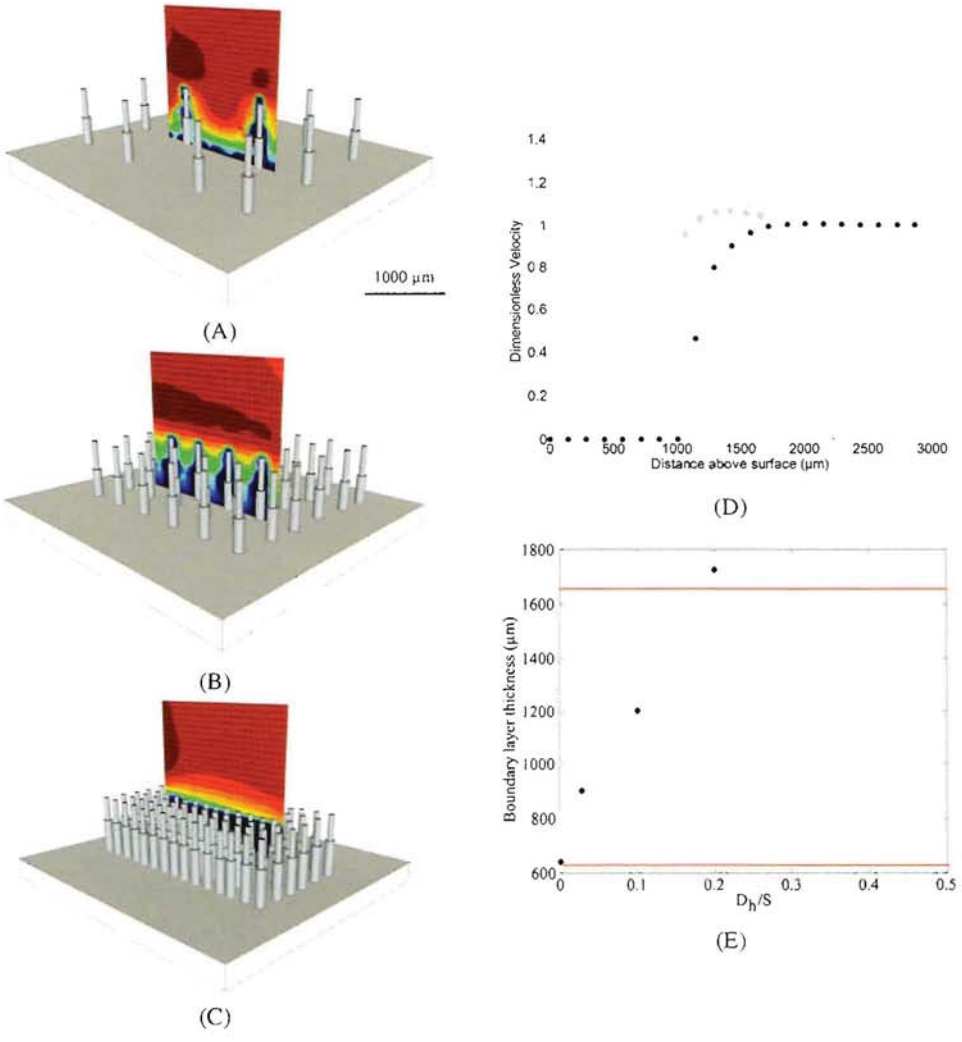

Fig. 11. PIV measurements of 2-dimensional flow velocities in the cross-section of a pair of hairs (hair-diameter D_h of 50 μm, hair-length L_h of 1000 μm) surrounded by other hairs in a 60 Hz oscillatory flow. (A) $N_{\text{hairs}} = 4 \times 4$ on 5000× 5000 μm^2, hair spacing S is 1700 μm. (B) $N_{\text{hairs}} = 9 \times 9$ on 5000× 5000 μm^2, hair spacing is 500 μm. (C) $N_{\text{hairs}} = 19 \times 19$ on 5000× 5000 μm^2, hair spacing is 250 μm. In the depicted cases only a subset of hairs is shown in order to give an impression. (D) Non-dimensional velocity profiles extracted as a function of the height above the surface, in between hairs for the 3 spacings (square, 1800 μm, grey circle, 500 μm, black circle 250 μm). (E) Estimation of the boundary layer thickness for the different spacing (D_h/S), $D_h/S = 0$ being the measurement of the flow on a flat plate and $D_h/S = 0.5$ corresponding to a sample with adjacent hairs.

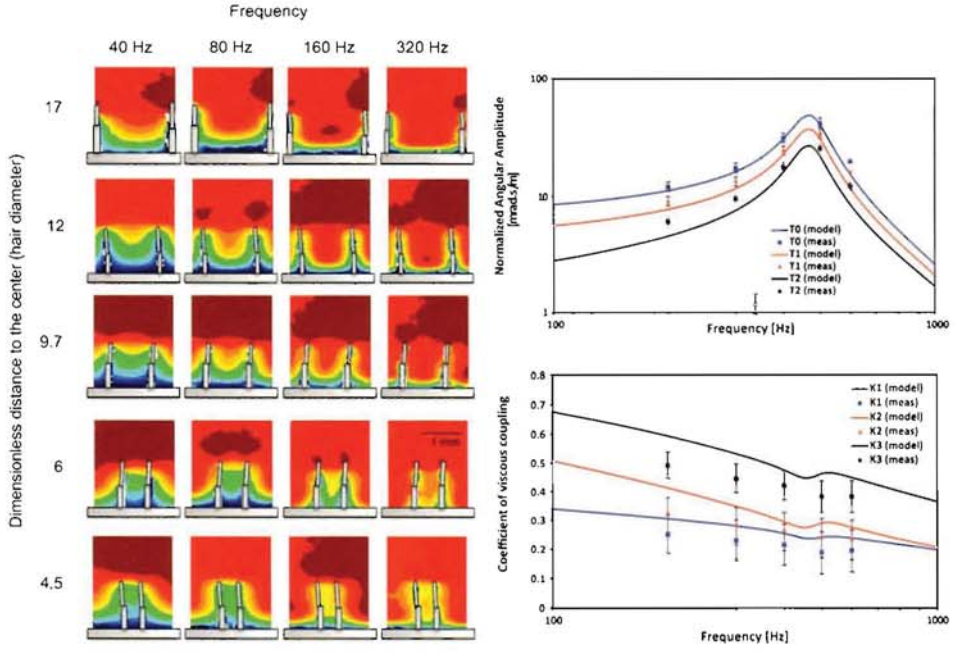

Fig. 12. Left: Spatial harmonic-flow amplitude-distributions for various inter-hair distances and frequencies. The normalized distance (D/S) between the hairs is indicated by the numbers left of the rows.[27] Right, top: Influence of inter-hair viscous coupling on hair-rotation amplitude. Right, bottom: Frequency dependence of the viscous coupling constant for 2 versus 0 perturbing hairs (black), 2 versus 1 perturbing hair (red) and 1 versus 0 perturbing hairs (blue). $D/S \approx 2.1$. Lines are predictions based on a modified model introduced in[31] in the limit of arrested hairs, dots are measurements with uncertainty intervals.

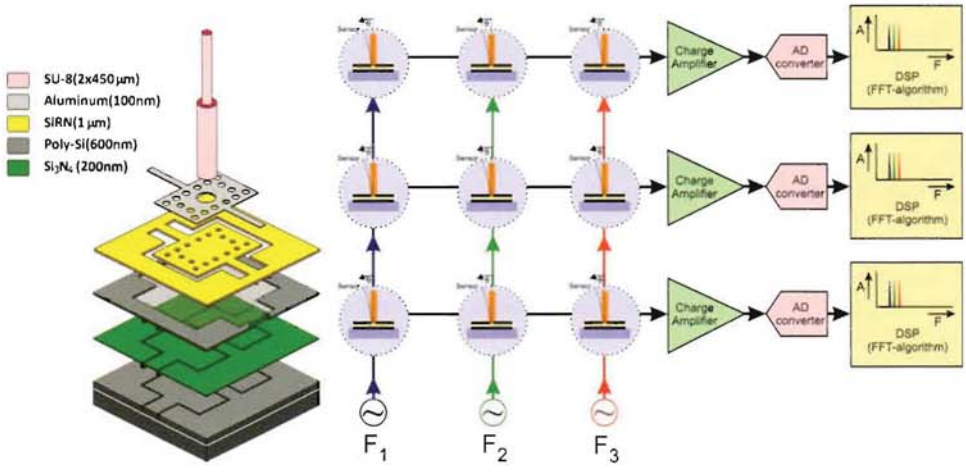

Fig. 13. Left: Extruded SOI-based hair-sensor structure.[19] Right: FDM reduces the number of electrical connections while retaining the original sensor SNR.[32]

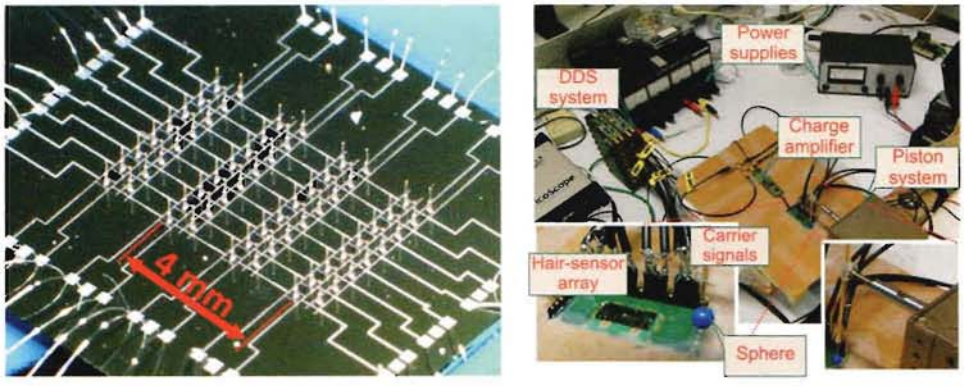

Fig. 14. Left: microphotograph of an 8 × 8 array of individually FDM addressable hair-sensors, ordered in pairs with orthogonal directivity.[32] Right: The setup used for transient measurements.

4.1. *Transient airflow measurements using artificial hair sensors*

For many insects airflow patterns, as observed by means of their hair-sensors, carry highly valuable information exposing the sources of these flows. The successful extraction of the characteristics of these spatio-temporal airflow patterns will give us insight in their features and information contained in them. In nature, there are numerous examples representing transient airflow stimuli such as spider motion[7] and (passing) humming flies.[33]

In most investigations on our artificial hair-sensors the measurements were conducted using sinusoidal airflows.[19] Obviously, using transient signals spatio-temporal information becomes richer and array-measurements will allow to capture important flow events. Here, we describe measurements of spatio-temporal airflow fields generated by a pulsed-like airflow by means of our artificial hair-sensor arrays.

4.2. *Measurements setup and results*

We measured responses of our biomimetic hair sensors to airflow transients using a sphere with 3 mm radius attached to a piston system to represent the motion of a spider at a distance (D) from the substrate. The sphere moves parallel to the x-axis. A single-chip array consisting of individually addressed (by FDM interfacing) hair sensors is used for flow-detection. Figure 14 (right) shows a photograph of the measurement setup.

Figure 15 shows an example of theoretical (left) and measured (right) hair-sensor responses due to the sphere movement. Interestingly, the hair-sensor response shows strong similarities with the theoretical dipole source field. The distance to the sphere is encoded in the characteristic points of the flow-field.[19] Hence, it can

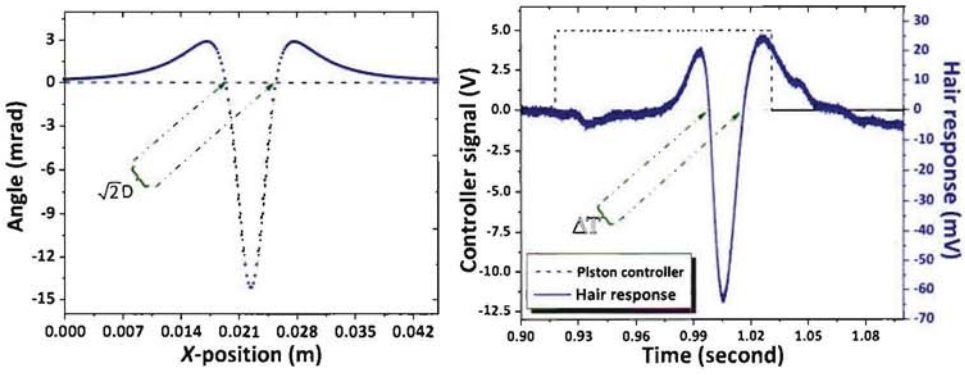

Fig. 15. Left: Theoretical transient dipole flow-field parallel to the direction of orientation of the flow-sensor. Right: An example of measured hair sensor response (solid) when exposed to a transient flow.

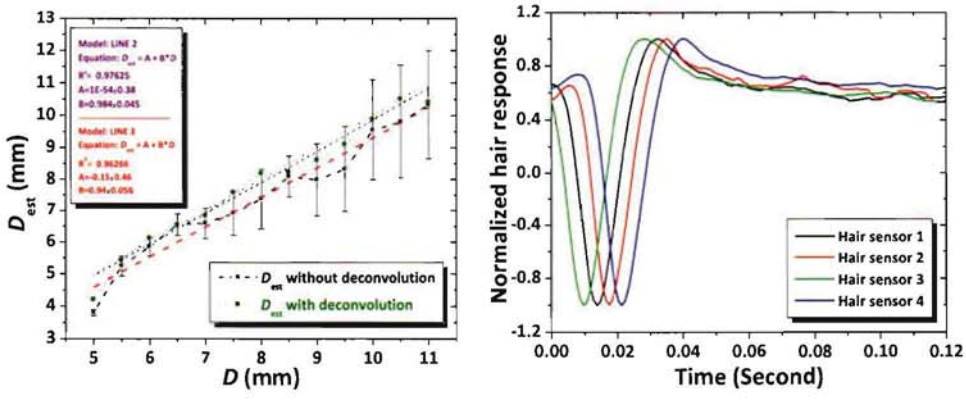

Fig. 16. Left: D_{est} versus D using transient hair-response measurements, before (solid-squares) and after (solid-circles) deconvolving the hair-sensor response. The best linear-line fit for both measurements are compared with ideal linear-line (dotted). D represents the height of the sphere center relative to the substrate. The error bars represent the uncertainty in determining the zero-crossing points of the measured dipole profile. Right: Normalized output of 4 simultaneously measured sensors when exposed to a sphere passing by at certain distance.[34]

be derived from the sensor output. In the transient response, the time difference between the characteristic points can be translated into position using the piston speed, and subsequently into an estimated distance (D_{est}) between sphere and hair sensor. Figure 16 (left) shows D_{est} versus D using the transient hair response.

To exclude effects of the hair-mechanics a deconvolution was performed to recover the flow-velocity. The results show that the deconvolved sensor data nearly matches the raw sensor data with a slight widening in its characteristic points. Hence,

we anticipate that the hair sensor is following the development of the flow profile rather well, a consequence of the nearly critical damped system with best frequency in the range of 250 Hz to 300 Hz. The results using the deconvolved sensor data (Fig. 16, left) indicate that the linear-line fit of D_{est} more closely matches the physical D while for the raw sensor data the D_{est} seems to closly resemble the distance to the center of the hair shaft. This highlights the effect of the mechanics and the hair-shaft of the sensor. Since we know of no way to correct for the integrated drag-force on the length of the hair we consider the torque as a reasonable representation of the flow field at between 1/2 and 2/3 the hair length (i.e., 600 μm to 700 μm above the substrate).

Arrays of hair sensors offer us spatial information, specifically if they are measured simultaneously. Here we integrated FDM to simultaneously measure the transient response of multiple hairs i.e., spatio-temporal airflow pattern measurements. Figure 16 (right) shows the response of four single-hair sensors in one row, when they are exposed to a transient airflow produced by a moving sphere.

Using the signal profiles as detected by an entire array would allow us to determine a number of source properties. By virtue of the piston velocity the delay represents the separation distance in between two hairs divided by the sphere velocity. Thus, the sphere velocity can be determined independently of the distance to the sphere. As a first trial, we determined the delays between the signals from four hairs in one row. As an example Fig. 16, right, displays the normalized responses for 4 hair-sensors in line where the sphere was moved along. The measurements show about 4 ms time delay between each two subsequent hair-sensor responses. From the sensor-responses and the distance between the sensors a speed of 512 mm/s at a distance of 5 mm to 7 mm was inferred.[34,35] This demonstrates the possibility to perform spatio-temporal flow pattern measurements using a single-chip hair sensor array with FDM and to, subsequently, use the features of these flow profiles to determine source parameters (i.e., size, speed and position).

Measurements like these, in principle, allow to extract the following information. (a) The projection of the velocity of the passing sphere in the direction parallel to the row of the sensor array can be determined using the distance between the sensors and the time of flight. (b) Once the velocity is known, the distance of the sphere trajectory perpendicular to the row of sensors can be determined from the characteristic points of the dipole-induced signal.[35] (c) With the distance to the sphere and its velocity known, the amplitude of the signal can be used to determine the size of the sphere. (d) Additional sensors allow to track the motion of the sphere in other directions as well. Clearly, the algorithm discussed above does not reflect the way crickets use their hair-sensor arrays but it is instructive to see which information an array of sensors in principle can uncover.

In conclusion, the individual responses of single hair-sensors within an array were measured simultaneously using FDM array interfacing, demonstrating the feasibility of high-resolution flow cameras. Source localization using the measured signals demonstrates what can be done with our hair-sensor arrays with respect to the detection of spatio-temporal airflow fields. The above results also can shed some light upon the mechanisms that are at work in crickets' flow sensing and which information is available in spatio-temporal airflow patterns to estimate the position and direction of moving objects in their close environment (both of which have been described in literature[7]).

5. Beyond Bio-Inspiration: Parametric Effects

Apart from using the capacitively interrogated hair-sensors strictly for sensing, one may achieve parametric effects by application of additional DC or AC bias-voltages to the electrodes (Fig. 17 left).

These voltages will produce electrostatic forces, which in a balanced situation (i.e., no tilt of the hair) do not change the rotational angle, but in a tilted situation will produce the largest forces on the side with the smallest gap. So, the electrostatic torque tends to add to the flow induced torque and therefore the applied voltages will serve as an electronic means to adaptively change the spring-stiffness of the hair-sensor system, i.e., electrostatic spring softening (ESS).

To model the system's behavior under application of symmetric bias voltages, we consider the electrostatically induced torque and stiffness which can be calculated from the first and second derivative of the energy in the capacitor with respect to θ respectively.

Due to the small angles θ encountered in practice and since the gap is much smaller than both the width w and length of the plates $2L$, the capacitor is treated

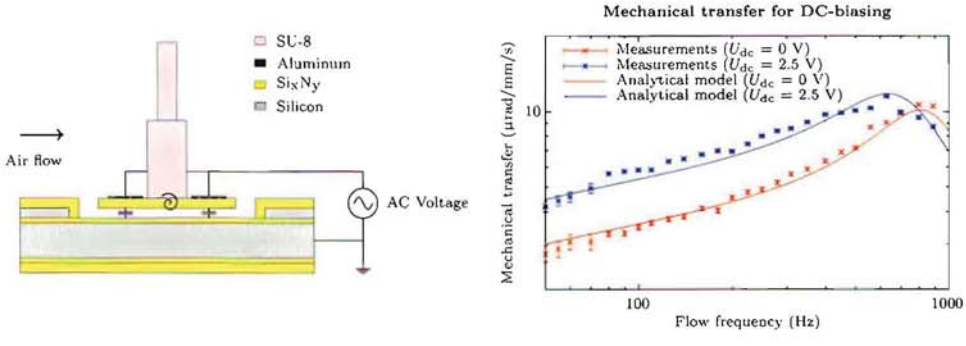

Fig. 17. Left: electrodes can also be exploited for electrostatic actuation. Right: improvement of the mechanical responsivity and reduction of the resonance frequency on DC-bias induced ESS.[36]

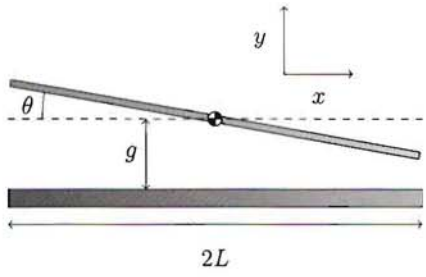

Fig. 18. Geometry of the angle-dependent rectangular capacitor.

as a parallel plate geometry (Fig. 18). The sensor operates in air, for which the relative electric permittivity is assumed to be equal to 1. Additionally, the two silicon-nitride layers with thicknesses t_1 and t_2, and relative permittivity ϵ_r increase the gap-distance, leading to an effective gap g_{eff}:

$$g_{\text{eff}} = g + \frac{t_1}{\epsilon_r} + \frac{t_2}{\epsilon_r}. \tag{13}$$

The angle dependent capacitance $C(\theta)$ for the rotational sensor using the parallel plate approximation is given by:

$$C(\theta) = \epsilon_0 w \frac{\cos(\theta)}{\sin(\theta)} \ln\left(\frac{g_{\text{eff}} + L\sin(\theta)}{g_{\text{eff}} - L\sin(\theta)}\right). \tag{14}$$

Transduction principles are used to find the ESS by an angle-dependent and voltage-controlled capacitor. For this, we use Legendre's transform for the co-energy E' of the system, since the capacitor is so-called voltage-controlled:

$$E'(\theta, u) = \frac{1}{2} S_0 \theta^2 - \frac{1}{2} u^2 C(\theta), \tag{15}$$

where S_0 is the intrinsic material-based stiffness. The effective stiffness is found by differentiating twice with respect to the rotational angle θ and keeping the voltage u constant:

$$S = \left.\frac{\partial^2 E'}{\partial \theta^2}\right|_u = S_0 - \frac{1}{2} u^2 \frac{\partial^2 C(\theta)}{\partial \theta^2}. \tag{16}$$

Hence, on applying a bias voltage u, the total torsional stiffness S becomes:

$$S = S_0 - \eta u^2 \quad \text{with } \eta \approx \frac{2\epsilon_0 w L^3}{3 g_{\text{eff}}^3}. \tag{17}$$

These expressions state that the total torsional stiffness S contains both the intrinsic material-based stiffness S_0 and a voltage-dependent stiffness, allowing for electrostatic control of the system's response.

5.1. *DC-biasing*

A DC-bias voltage can be used to change the system's torsional stiffness. Experimentally the mechanical transfer is determined for flow frequencies from 100 Hz to 1000 Hz with and without the application of a DC-bias voltage. During this measurement, a DC-bias voltage U_{dc} of 2.5 V is used, giving an increase in sensitivity of about 80% for frequencies within the sensor's bandwidth. Also lowering of the resonance frequency ω_r is observed (about 20%). Overall, measurements are in good agreement with modeling and it is shown clearly that DC-biasing leads to a larger sensitivity below the sensor's resonance frequency and a decrease of the resonance frequency (Fig. 17 right).[36]

5.2. *Parametric amplification*

To improve the performance of these sensors even further and implement adaptive filtering, we make use of non-resonant parametric amplification (PA). PA is a mechanism based on modulation of one or more system parameters, in order to control the system behavior. This leads to complex interactions between the modulating signals in which amplitude, frequency and phase play important roles.[37] We obtained the conditions for PA in our hair-sensor system by changing the DC-bias voltage to an AC-bias voltage (also called pump signal),[38] which is another way of exploiting ESS.

PA can give selective gain or attenuation, depending on the pump frequency f_p and pump phase ϕ_p. Equal frequencies for flow and pump ($f_p = f_a$) give coherency in torque and spring softening, for which the pump phase determines whether the system will show relative amplification or attenuation. Therefore, it is possible to realize a very sharp band pass/stop filter, depending on the pump settings.

Setting the frequency of the AC-bias voltage to 150 Hz, its amplitude to 5 V and the pump phase to the value producing maximum gain, and supplying an oscillating air flow consisting of three frequency components (135 Hz, 150 Hz, 165 Hz), filtering and selective gain of the flow signal are demonstrated, see Fig 19, left . The presence of a bias-signal, through the action of non-resonant PA, increases the frequency-matched signal by 20 db, whereas the other two components are only amplified by 8 to 9 db, resulting in selective gain of the flow signal.[38]

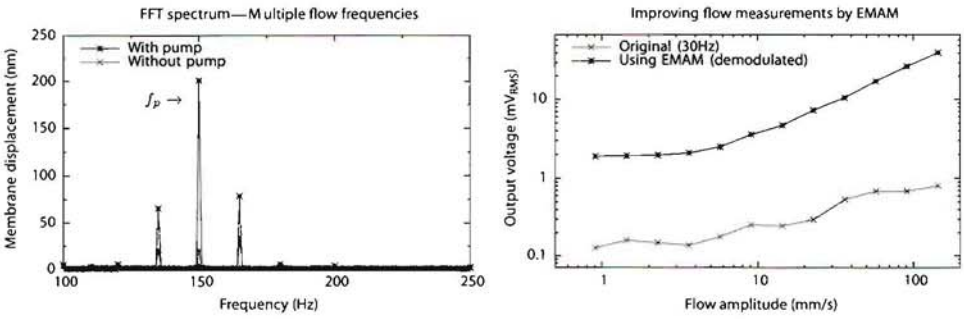

Fig. 19. Left: Measured gain of about 20 db for the flow frequency component at 150 Hz determined by FFT. The AC-bias voltage is fixed at $f_p = 150$ Hz with an amplitude of 5 V. Right: Improvement of the quality of the measured RMS-voltage values at low frequency signals using Electro Mechanical Amplitude Modulation (EMAM). In case of EMAM, a clear linear relationship between flow and output voltage is observed above the system's noise level (> 5 mm/s).

5.3. *EMAM*

We also implemented ESS by setting the AC-bias voltage frequency considerably higher than the frequency of the air flow. As a result, the system's spring-stiffness is electromechanically modulated, which results in EMAM. Experimentally, generating a harmonic flow at 30 Hz and setting the AC-bias voltage frequency to 300 Hz the flow is modulated and the flow information is upconverted to higher frequencies.[39]

The incoming air flow signal is recovered by demodulation (using synchronous detection) of the measured rotational angle. Without EMAM, a noisy relationship between the flow amplitude and the resulting output voltage is observed. Also, large, undesired, fluctuations are observed (Fig. 19, right). However, with EMAM, a clear linear relationship is observed for flow velocity amplitudes above 5 mm/s, showing that the measurement quality of low frequency flows too can be improved by ESS.

6. Summary and Conclusions

Crickets possess a sensitive, distributed hair-sensor system with near to thermal-mechanical noise-threshold sensitivities and which forms an interesting example system for sensory-system engineering. Engineers and biologists working together on this system have been able to make artificial hair-sensor systems and quantify the effects of viscosity mediated coupling. Interfacing arrays of sensors by means of FDM has delivered systems with simultaneous read-out of many sensors and which can be used as flow-cameras. The electrode structures used for capactive read-out

also allow for actuation of the hair-sensors and enable such exciting schemes as PA and filtering, adaptive-reversible sensor-tuning and electromechanical amplitude modulation (frequency shifting of signals). Future work will also encompass studies on the use of stochastic resonance and application of our technology to other bioinspired sensing modalities.

Despite all advancements in artificial hair-sensor systems the biological example still is far more complex, evolved and capable, e.g., the full 3-dimensional shape of the cricket cerci, the large number of innervated hairs, the robust generation of neural signals and subsequent intricate processing in the TAG are still far from feasible with current technology. And even if this were technologically possible still many questions regarding the cricket flow-sensing system are unanswered, holding both challenges and promises for the future.

Acknowledgments

The authors would like to thank STW/NWO for funding this research in the framework of the Vici project BioEARS and the EU for funding the Cicada and Cilia projects. Contributions from T. Lammerink and R. Wiegerink have been invaluable. E. Berenschot, M. de Boer, R. Sanders and H. van Wolferen have given technical support without which this work would not have existed. Numerous students have contributed to this research, for which they are gratefully acknowledged.

References

1. T. Shimozawa, J. Murakami and T. Kumagai, Cricket wind receptors: Thermal noise for the highest sensitivity known, in *Sensors and Sensing in Biology and Engineering*, F. G. Barth, J. A. C. Humphrey and T. W. Secomb (eds.) (Springer, 2003), pp. 145–159.
2. J. A. Humphrey and F. G. Barth, Medium flow-sensing hairs: Biomechanics and models, in *Advances in Insect Physiology*, S. Simpson (ed.) (Elsevier, 2008), pp. 1–80.
3. J. P. Miller, S. Krueger, J. J. Heys and T. Gedeon, *PLoS ONE* **6**(11), e27873 (2011).
4. J. J. Heys, P. K. Rajaraman, T. Gedeon and J. P. Miller, *PLoS ONE* **7**(10), e46588 (2012).
5. O. Dangles, T. Steinmann, D. Pierre, F. Vannier and JérômeCasas, *J Comp Physiol A* **194**, 653–663 (2008).
6. G. A. Jacobs, J. P. Miller and Z. Aldworth, *J Exp Biol* **211**, 1819–1828 (2008).
7. O. Dangles, N. Ory, T. Steinmann, J. P. Christides and J. Casas, *Anim Behav* **72**, 603–610 (2006).
8. H. Lamb, *The Dynamical Theory of Sound* (Edward Arnold, London, 1910).
9. R. Kant and J. A. C. Humphrey, *J R Soc Interface* **6**(6), 1047–1064 (2009).
10. J. Tautz and H. Markl, *Behav Ecol Sociobiol* **4**, 101–110 (1978).
11. J. Humphrey, R. Devarakonda, I. Iglesias and F. Barth, *Phil Trans Bio Sc* **340**, 423–444 (1993).
12. T. Shimozawa, T. Kumagai and Y. Baba, *J Comp Physiol A* **183**, 171–186 (1998).
13. R. L. Panton, *Incompressible Flow* (Wiley, 1996).
14. G. G. Stokes, *Trans Cambr Phil Soc* **9**, 1–141 (1851).

15. R. Jaganatharaja, C. Bruinink, B. Hagedoorn, M. Kolster, T. Lammerink, R. Wiegerink and G. Krijnen, *Proc Transducers 2009*, pp. 1541–1544, Denver, USA (June 21–25, 2009).
16. M. McConney, C. Schaber, M. Julian, F. Barth and V. Tsukruk, *J R Soc Interface* **4**, 1135–1143 (2007).
17. B. Bathellier, T. Steinmann, F. G. Barth and J. Casas, *J R Soc Interface* **9**(71), 1131–1143 (2012).
18. G. Krijnen, T. Lammerink, R. Wiegerink and J. Casas, *Proc IEEE Sensors 2007*, pp. 539–546, Atlanta, USA (October 28–31, 2007).
19. A. Dagamseh, C. Bruinink, H. Droogendijk, R. Wiegerink, T. Lammerink and G. Krijnen, *Proc IEEE Sensors 2010*, pp. 2251–2254, Waikoloa, Hawaii, USA (November 1–4, 2010).
20. T. Shimozawa and M. Kanou, *J Comp Physiol A* **155**, 495–505 (1984).
21. W. Gnatzy, *Cell Tiss Res* **187**, 1–24 (1978).
22. J. J. van Baar, M. Dijkstra, R. J. Wiegerink, T. S. J. Lammerink and G. J. M. Krijnen, *Proc IEEE Sensors 2003*, pp. 332–336, Toronto, Canada (October 22–24, 2003).
23. M. Dijkstra, J. J. J. van Baar, R. J. Wiegerink, T. S. J. Lammerink, J. H. de Boer and G. J. M. Krijnen, *J Micromech Microeng* **15**, S132–S138 (July, 2005).
24. H.-C. Huang and C.-C. Fu, *IEEE Sensors 2005*, pp. 484–487, Irvine, USA (October 30–November 3, 2005).
25. K. Kim, D. S. Park, H. M. Lu, W. Che, K. Kim, J.-B. Lee and C. Ahn, *J Micromech Microeng* **14**, 597–603 (2004).
26. H. Yu, K. Shibata, B. Li and X. Zhang, *Proc Miniaturized Systems for Chemistry and Life Sciences*, pp. 187–189, Boston, USA (October 9–13, 2005).
27. J. Casas, T. Steinmann and G. Krijnen, *J R Soc Interface* **7**(51), 1487–1495 (2010).
28. G. C. Lewin and J. Hallam, *J Comp Physiol A* **196**, 385–395 (2010).
29. J. Mulder-Rosi, G. Cummins and J. Miller, *J Neurophys* **103**(4), 1823–1832 (2010).
30. R. Jaganatharaja, H. Droogendijk, S. Vats, B. Hagedoorn, C. Bruinink and G. Krijnen. *Proc MEMS 2011*, pp. 652–655, Cancun, Mexico (January 23–27, 2011).
31. B. Bathellier, F. Barth, J. Albert and J. Humphrey, *J Comp Physiol A* **191**, 733746 (2005).
32. A. Dagamseh, T. Lammerink, R. Sanders, R. Wiegerink and G. Krijnen, *Proc MEMS 2011*, pp. 648–651, Cancun, Mexico (January 23–27, 2011).
33. F. G. Barth, J. A. H. U. Wastl, J. Halbritter and W. Brittinger, *Phil Trans R Soc B* **347**, 397–412 (1995).
34. A. M. K. Dagamseh, R. J. Wiegerink, T. S. J. Lammerink and G. J. M. Krijnen, *Bioinsp Biomim* **7**, 046009 (2012).
35. J. Franosch, A. Sichert, M. Suttner and J. V. Hemmen, *Biol Cybernetics* **93**, 231–238 (2005).
36. H. Droogendijk, C. M. Bruinink, R. G. P. Sanders, A. M. K. Dagamseh, R. J. Dagamesh and G. J. M. Krijnen, *J Micromech Microeng* **22**(6), 065026 (2012).
37. D. Rugar and P. Grütter, *Phys Rev Lett* **67**, 699–702 (1991).
38. H. Droogendijk, C. M. Bruinink, R. G. P. Sanders and G. J. M. Krijnen, *Appl Phys Lett* **99**, 213503 (2011).
39. H. Droogendijk, C. M. Bruinink, R. G. P. Sanders and G. J. M. Krijnen, *Proc MEMS 2012*, pp. 531–534, Paris, France (January 29–February 2, 2012).

Handbook of Biomimetics and Bioinspiration

② Electromechanical Systems

Global warming, pollution, food and water shortage, cyberspace insecurity, over-population, land erosion, and an overburdened health care system are major issues facing the human race and our planet. These challenges have presented a mandate to develop "natural" or "green" technologies using nature and the living system as a guide to rationally design processes, devices, and systems. This approach has given rise to a new paradigm, one in which innovation goes hand-in-hand with less waste, less pollution, and less invasiveness to life on earth. Bioinspiration has also led to the development of technologies that mimic the hierarchical complexity of biological systems, leading to novel highly efficient, more reliable multifunctional materials, devices, and systems that can perform multiple tasks at one time. This multi-volume handbook focuses on the application of biomimetics and bioinspiration in medicine and engineering to produce miniaturized multi-functional materials, devices, and systems to perform complex tasks. Our understanding of complex biological systems at different length scales has increased dramatically as our ability to observe nature has expanded from macro to molecular scale, leading to the rational biologically-driven design to find solution to technological problems in medicine and engineering.

The following three-volume set covers the fields of bioinspired materials, electromechanical systems developed from concepts inspired by nature, and tissue models respectively.

- 1: Bioinspired Materials
- 2: Electromechanical Systems
- 3: Tissue Models

This three-volume set is a must-have for anyone keen to understand the complexity of biological systems and how that complexity can be mimicked to engineer novel materials, devices and systems to solve pressing technological challenges of the twenty-first century.

This book (2) is the second volume of the set. It presents nature-oriented studies and developments in the field of electromechanical devices and systems. These include actuators and robots based on the movement of muscles, algal antenna and photoreception; the non-imaging light sensing system of sea stars; the optical system of insect ocellus; smart nanochannels and pumps in cell membranes; neuromuscular and sensory devices that mimic the architecture of peripheral nervous system; olfaction-based odor sensing; cilia-mimetic microfluidic systems; the infrared sensory system of pyrophilous insects; ecologically inspired multizone temperature control systems; cochlea and surface acoustic wave resonators; crickets' cercal system and flow sensing abilities; locusts' wings and flapping micro air vehicles; the visual motion sensing of flying insects; hearing aid devices based on the human cochlea; the geometric perception of tortoises and pigeons; the organic matter sensing capability of cats and dogs; and the silent flight of rats.

World Scientific
www.worldscientific.com
8169 hc

ISBN 978-981-4354-92-9 (set)
9 789814 354929

ISBN 978-981-4354-95-0 (v2)
9 789814 354950